


## Active terahertz spin state and optical chirality in liquid crystal chiral metasurface

Yunyun Ji <sup>1</sup>, Fei Fan,<sup>1,\*</sup> Ziyang Zhang,<sup>2</sup> Zhiyu Tan,<sup>1</sup> Xin Zhang,<sup>1</sup> Yiwu Yuan,<sup>1</sup> Jierong Cheng,<sup>1</sup> and Shengjiang Chang<sup>2,†</sup>

<sup>1</sup>*Institute of Modern Optics, Nankai University, Tianjin Key Laboratory of Micro-scale Optical Information Science and Technology, Tianjin 300350, China*

<sup>2</sup>*Tianjin Key Laboratory of Optoelectronic Sensor and Sensing Network Technology, Tianjin 300350, China*



(Received 6 April 2021; accepted 19 July 2021; published 3 August 2021)

Dynamic control of photonic spin state and chirality plays a vital role in various applications, such as polarization control, polarization-sensitive imaging, and biosensing. Here, we present a scheme for the flexible and dynamic manipulation of terahertz spin state conversion and optical chirality by combining two achiral structures: an asymmetric metasurface and a layer of anisotropic liquid crystal. The proposed asymmetric metasurface can realize the polarization conversion effect. For the circularly polarized incidence, it exhibits the asymmetric transmission of the spin-flipped states but no spin-locked optical chirality since its geometry is mirror symmetric along with the wave propagation. The introduction of the liquid crystal makes the composite metasurface not only exhibit the spin state conversion but also spin-locked chirality and spin-flipped chirality on account of breaking mirror symmetry, which realizes an electrically active terahertz chiral device. The experimental results show that the asymmetric transmission of the terahertz spin states can be dynamically manipulated, resulting in a large controllable range 83.8% to  $-30.7\%$  of spin-locked circular dichroism at 0.76 THz and  $-98.2\%$  to 44.7% of spin-flipped circular dichroism at 0.73 THz. This work paves the way for the development of terahertz meta devices capable of enabling active photonic spin state and chirality manipulation.

DOI: [10.1103/PhysRevMaterials.5.085201](https://doi.org/10.1103/PhysRevMaterials.5.085201)

### I. INTRODUCTION

Chirality is a quite ubiquitous phenomenon throughout the universe, ranging from molecules and amino acids to galaxies in the universe. Usually, the structures lacking any mirror plane or inversion symmetry are called chiral objects, which can exhibit different optical responses to the circularly polarized (CP) light with different photonic spin states and result in chiroptical effects [1–5]. The chiroptical effects can be described quantitatively by circular dichroism (CD), i.e., the differential absorbance under the two CP illuminations with different handedness, and optical activity (OA), i.e., the polarization rotation of a linearly polarized (LP) light through chiral media [6–8]. However, the chiroptical effects in most natural chiral media are extremely small; to obtain sufficient optical chirality, the optical devices need to be bulkier, which is not conducive to the integration and miniaturization of the device, thus hampering their practical applications [9].

Artificial metamaterials are a new class of composite materials, which have the advantages of flexible design, simple fabrication, ultrathin size, and easy integration. A lot of works have been reported on chiral metamaterials in the optical [10,11], infrared [12,13], terahertz (THz) [14,15], and microwave [16,17] regimes. An outstanding feature of chiral metamaterials is the enhanced chiroptical responses that are several orders of magnitude stronger than natural materi-

als due to breaking mirror symmetry in geometry [18–21]. Nevertheless, the chiroptical effects of those chiral metamaterials are fixed once they are fabricated, and lack dynamic tunability. A good strategy is to introduce functional materials, such as phase change materials [22], graphene [23], and liquid crystal (LC) materials [24], that can respond to the thermal, optical, electric, or magnetic field. Thus, the unique tunable characteristics of the above functional materials allow the active and flexible control of optical chirality when integrated with chiral metamaterials.

THz waves are typically defined as electromagnetic waves spanning from 0.1 to 10 THz. Thanks to low photon energy and low noise interference, THz spectroscopy technology is an effective noninvasive and nondestructive testing method [25–28]. In particular, THz optical chiral technology, an important complementary tool to THz absorption spectroscopy technology, has been developed to understand and identify chiral biomaterials [29,30]. Consequently, THz chiral metamaterials, especially those integrated with functional materials with active tunability, not only dynamically control the polarization state and chirality of THz waves but offer multifaceted spectroscopic capabilities for understanding the chiral architecture in biomaterials. Generally, the excitation of free carriers in graphene, semiconductor, and phase change materials under strong light illumination can be used to dynamically control THz chirality [31–37]. For example, the dynamically tunable chiroptical responses at THz frequencies were demonstrated in hybrid metamaterials integrated with the vanadium dioxide (VO<sub>2</sub>) under the thermal excitation [34,35]. Kim *et al.* reported that an active modulation of THz CD from 14 to 45 dB at 1.1 THz was achieved by electrically

\*fanfei@nankai.edu.cn

†sjchang@nankai.edu.cn

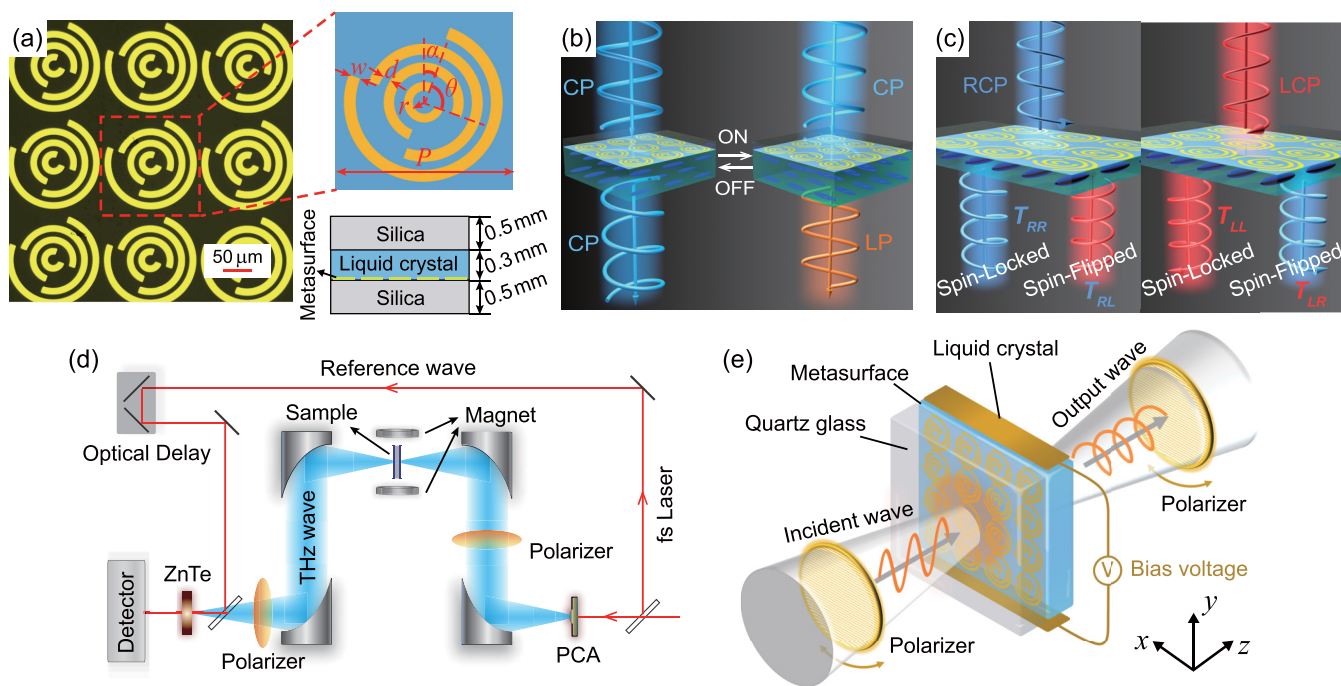


FIG. 1. (a) Optical microscope photo and geometric parameters of the metasurface. (b) Schematic diagram of dynamically controllable polarization conversion. (c) Schematic diagram of the spin-locked states and spin-flipped states. (d) Schematic diagram of the THz-TDPS system. (e) Experimental setup for polarization and phase measurement.

controlled graphene [36]. However, the strong chiroptical response, larger tuning range, and more flexible control method for THz chiral devices are still in challenge.

As a functional material, LCs have large optical anisotropy that can be flexibly manipulated by thermal, optical, electric, or magnetic fields. The strategy of combining LCs with metasurfaces has been used in tunable THz functional devices, such as polarization converters, phase modulators, tunable waveplates, and spatial light modulators [38–44]. For example, Shen *et al.* demonstrated a dynamic Fano cloaking in a 250- $\mu\text{m}$ -thick LC layer integrated THz metasurface, and its modulation depth reaches over 50% in a broad frequency range of 660 GHz [39]. Some work on the tunable beam steering using reconfigurable metasurfaces coupled with LCs has been studied [40,41]. An ultrathin large-area THz spatial phase modulator was demonstrated at 0.8 THz with the thickness of the LC layer only 12  $\mu\text{m}$  ( $\sim 0.03\lambda$ ), the driving voltage as low as 20 V, and a spatial resolution of 85  $\mu\text{m}$  (better than  $0.23\lambda$ ) [42]. Recently, the cholesteric LCs have been reported to achieve strong THz OA and CD, and the strongest THz CD of 22 dB occurs around 250 K [44]. It can be predicted that the introduction of LCs to chiral metamaterials may be a feasible solution to dynamically control the chirality and spin state conversion of THz waves, yet related work is very rare.

In this work, we theoretically and experimentally investigate the spin state conversion and chirality of the composite LC chiral metasurface, which is an asymmetric metasurface filled with a layer of anisotropic LC. Benefit from the polarization conversion effect of the asymmetric metasurface and the electrically tunable anisotropic characteristics of the LCs, the THz spin state conversion of the composite LC chiral metasurface can be controlled between CP to CP and CP to LP

states. Besides, two kinds of asymmetric transmission for the THz spin states occur in the composite structure as it breaks mirror symmetry, which can be dynamically controlled. This LC chiral metasurface provides an efficient approach to dynamically manipulate the spin state conversion and optical chiral transmission of THz waves.

## II. METHODS

### A. Device design and fabrication

Here, we design and fabricate a planar metasurface consisting of four split rings as shown in Fig. 1(a), which breaks the rotational symmetry in the plane, so it can achieve the polarization conversion effect. Figure 1(b) shows the schematic diagram that the polarization conversion can be flexibly manipulated by electrically controlling the optical axis of the anisotropic material LCs. Moreover, the THz spin states can also be dynamically controlled, as shown in Fig. 1(c).

The planar asymmetric metasurface is fabricated on a glass substrate using the electron-beam lithography and lift-off technique. The 200-nm-thick metal film is deposited on the surface of the 500- $\mu\text{m}$ -thick JGS1 quartz glass substrate. Figure 1(a) shows the optical microscope photo and geometric parameters of this asymmetric metasurface, where  $w = 10 \mu\text{m}$ ,  $d = 10 \mu\text{m}$ , the inner radius of the first split ring  $r = 10 \mu\text{m}$ , the opening angle of each split ring  $\theta = 90^\circ$ ,  $\alpha = 20^\circ$ , and the lattice period  $P = 170 \mu\text{m}$  in both the  $x$ - and  $y$ -axis directions. Then, we package a layer of LC on the surface of the metasurface, and its cross section is shown in the inset of Fig. 1(a). The LC used in this paper is a mixture of E7 LC, which is obtained from Jiangsu Hecheng Technology Co., Ltd. The E7 LC is added to fill a 0.3-mm-thick LC cell, which

is fabricated by two parallel copper wires sandwiched within the planar asymmetric metasurface and a 500- $\mu\text{m}$ -thick quartz glass substrate.

### B. Experimental methods

A THz time-domain polarization spectroscopy (THz-TDPS) system is used in this experiment, and the schematic diagram is shown in Fig. 1(d). A low-temperature-grown GaAs photoconductive antenna is used to generate the incident THz pulses, which is excited by a Ti:sapphire laser with 75 fs duration of 80 MHz repetition rate working at 800 nm. The polarization direction of the incident THz wave is along the  $y$  axis. The sample is placed at the focal point of the THz-TDPS system. The two additional THz polarizers are placed in front of and behind the sample. The former is used to generate two orthogonal incident LP waves, which can synthesize a pair of orthogonal CP waves. The latter is used to obtain two orthogonal polarization components of the output wave. Thereby, we can detect the output wave with any polarization state, and then obtain its complete amplitude, phase, and polarization information. A 100-mT constant magnetic field is used for the pre-orientation treatment of LC molecules. The variable electric field is used to control the orientation of LC molecules, and the 9-mm gap between two electrodes ensures that the electrodes do not affect the transmission of THz waves, as shown in Fig. 1(e).

In this work, we are concerned about the output of two orthogonal THz spin components, namely the left-handed circularly polarized (LCP) and right-handed circularly polarized (RCP) components with different amplitudes and phases. If we can obtain the transmission amplitude ( $A_{+45^\circ}$ ,  $A_{-45^\circ}$ ) and the phase ( $\varphi_{+45^\circ}$ ,  $\varphi_{-45^\circ}$ ) for the  $+45^\circ$  and  $-45^\circ$  LP components by rotating the second THz polarizer, the amplitude transmission of RCP and LCP components can be given by

$$\begin{aligned} \begin{pmatrix} E_{\text{RCP}} \\ E_{\text{LCP}} \end{pmatrix} &= \frac{1}{\sqrt{2}} \begin{pmatrix} 1 & i \\ 1 & -i \end{pmatrix} \begin{pmatrix} E_{+45^\circ} \\ E_{-45^\circ} \end{pmatrix} \\ &= \frac{1}{\sqrt{2}} \begin{pmatrix} 1 & i \\ 1 & -i \end{pmatrix} \begin{pmatrix} A_{+45^\circ} e^{i\varphi_{+45^\circ}} \\ A_{-45^\circ} e^{i\varphi_{-45^\circ}} \end{pmatrix}. \end{aligned} \quad (1)$$

$$\mathbf{T}_{\text{circ}} = \begin{pmatrix} t_{RR} & t_{RL} \\ t_{LR} & t_{LL} \end{pmatrix} = \frac{1}{2} \begin{pmatrix} t_{++45^\circ} + t_{--45^\circ} + i(t_{+-45^\circ} - t_{-+45^\circ}) & t_{++45^\circ} - t_{--45^\circ} - i(t_{+-45^\circ} + t_{-+45^\circ}) \\ t_{++45^\circ} - t_{--45^\circ} + i(t_{+-45^\circ} + t_{-+45^\circ}) & t_{++45^\circ} + t_{--45^\circ} - i(t_{+-45^\circ} - t_{-+45^\circ}) \end{pmatrix}, \quad (5)$$

where  $R$  and  $L$  represented RCP and LCP light, and  $+45^\circ$  and  $-45^\circ$  were orthogonal LP components oriented in the  $+45^\circ$  and  $-45^\circ$  directions, respectively. According to Eq. (5), the amplitude and phase information of the above four spin states can be obtained in the experiment. To reflect the optical chirality response of the device, two chiral parameters (i.e., CD and OA) need to be defined:

$$\begin{aligned} \text{spin-locked CD} &= \frac{T_{RR} - T_{LL}}{T_{RR} + T_{LL}} \times 100\%, & \text{OA}(\circ) &= \frac{1}{2}(\varphi_{RR} - \varphi_{LL}), \\ \text{spin-flipped CD} &= \frac{T_{LR} - T_{RL}}{T_{LR} + T_{RL}} \times 100\%, & \text{OA}(\circ) &= \frac{1}{2}(\varphi_{LR} - \varphi_{RL}), \end{aligned} \quad (6)$$

where  $\varphi_{RR}$ ,  $\varphi_{LL}$ ,  $\varphi_{LR}$ , and  $\varphi_{RL}$  represent the phase,  $T_{RR}$ ,  $T_{LL}$ ,  $T_{LR}$ , and  $T_{RL}$  are the intensity transmissions expressed in dB. The spin-locked CD and OA reflect the asymmetry transmission between the spin-locked states, the CD shows the inten-

To intuitively describe the arbitrary polarization state of the output light, we calculated the terminal trajectory equation of electric vector  $\mathbf{E}$ , that is, polarization ellipse, as follows [45]:

$$\left(\frac{E_x}{A_{+45^\circ}}\right)^2 + \left(\frac{E_y}{A_{-45^\circ}}\right)^2 - \frac{2E_x E_y}{A_{+45^\circ} A_{-45^\circ}} \cos \Delta\varphi = \sin^2 \Delta\varphi, \quad (2)$$

where the phase difference  $\Delta\varphi = \varphi_{+45^\circ} - \varphi_{-45^\circ}$ . Then, the two polarization parameters, that is the ellipticity  $\chi$  and the polarization rotation angle  $\beta$ , can be obtained by

$$\chi = T_{\text{RCP}}(\text{dB}) - T_{\text{LCP}}(\text{dB}), \quad (3)$$

$$\beta = 0.5 \arctan(\tan 2\varepsilon \cos \Delta\varphi), \quad (4)$$

where  $T_{\text{RCP}}(\text{dB}) = 20 \times \log_{10} |E_{\text{RCP}}|$  and  $T_{\text{LCP}}(\text{dB}) = 20 \times \log_{10} |E_{\text{LCP}}|$  are the intensity transmission expressed in dB of RCP and LCP components, and  $\tan \varepsilon = A_{+45^\circ} - A_{-45^\circ}$ .

However, the above parameters cannot fully reflect the transmission characteristics of the experimental system. If the incident wave is an LP wave and the output is an RCP wave, it may be transmitted directly by the RCP component or converted from the LCP wave. As a consequence, for a pair of orthogonal spin states, it is necessary to distinguish the co-polarization transmission and the cross-polarization transmission cases. As shown in Fig. 1(c), the co-polarization transmission yields the spin-locked states ( $t_{RR}$ ,  $t_{LL}$ ) and the cross-polarization transmission yields the spin-flipped states ( $t_{RL}$ ,  $t_{LR}$ ), where the first subscript indicates the polarization state of the output component, and the latter represents the polarization state of the input wave.

To obtain the transmission coefficients of CP waves (that is,  $t_{RR}$ ,  $t_{RL}$ ,  $t_{LR}$ ,  $t_{LL}$ ), we need to measure four linearly co- and cross-polarized transmission coefficients  $t_{++45^\circ}$ ,  $t_{+-45^\circ}$ ,  $t_{-+45^\circ}$ ,  $t_{--45^\circ}$  by rotating two THz polarizers. Therefore, the transmission coefficients of CP light in a circular base can be described based on the LP states coefficient in the Cartesian base as [46,47]

sity difference, and OA represents the phase shift. Similarly, the spin-flipped CD and OA reflect the asymmetry transmission between the spin-flipped states. These four parameters can fully characterize the optical chirality of the device.

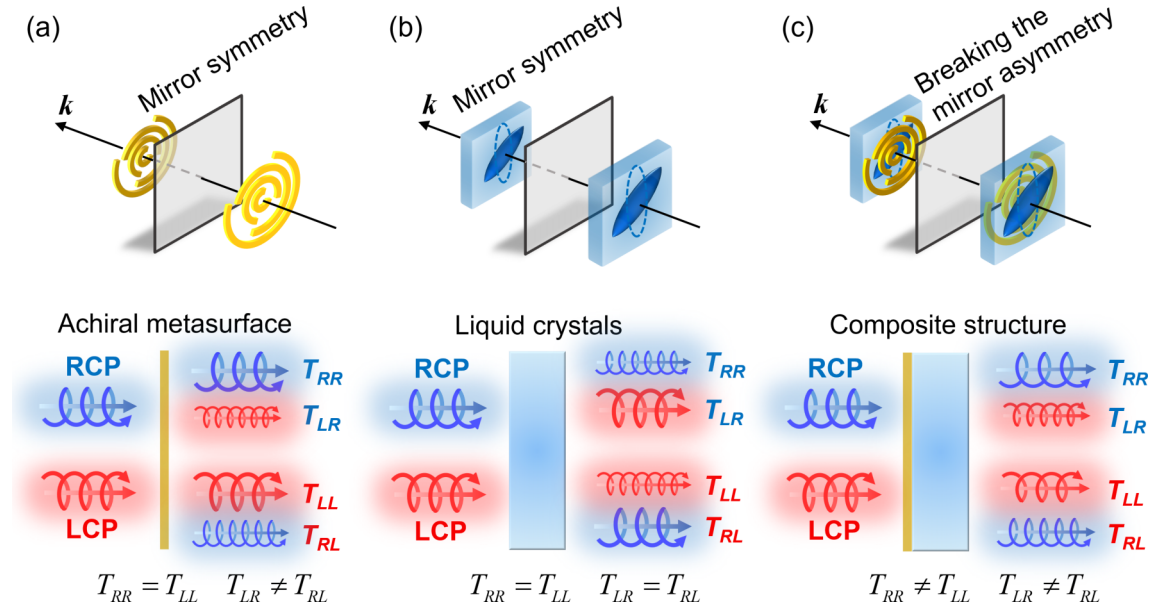


FIG. 2. Schematic diagram of the geometric symmetry in the propagation direction and the transmission of CP light for the single asymmetric metasurface (a), the single LC layer (b), and the composite LC chiral metasurface (c).

### C. Numerical simulation

Numerical simulations are modeled by using commercially available software tools based on the Finite-Difference Time-Domain (FDTD) method. The periodic boundary conditions are applied in the  $x$  and  $y$  directions. The  $z$  boundary is surrounded by perfectly matched layers. The period in both the  $x$  and  $y$  directions is  $170 \mu\text{m}$ , and the modeling length in the  $z$  direction (the direction of the incoming light) is  $2.5 \text{ mm}$ . The glass permittivity is set to  $3.61$ . The metal structure used in the simulations is set to a perfect electrical conductor (PEC), and it is safe to consider the metal as the perfect electric conductor in the range of considered THz frequencies [48]. The minimum mesh step in this simulation model is set to  $dx = dy = 5 \mu\text{m}$  ( $\sim\lambda/30$ ) and  $dz = 2.315 \mu\text{m}$  ( $\sim\lambda/60$ ), which is much smaller than the wavelength of THz wave and the size of the structure, and the time step is  $0.026 \text{ ps}$ . The LC is modeled as a uniaxial material, and its optical axis can be rotated in the  $x$ - $y$  plane; the extraordinary and ordinary refractive indices ( $n_e$  and  $n_o$ ) are set to  $1.78$  and  $1.6$ , respectively. Besides, the LCP and RCP sources are generated using two orthogonal LP sources with a  $\pm 90^\circ$  phase change.

## III. RESULTS AND DISCUSSION

### A. Polarization conversion of asymmetric metasurface without LCs

First, we analyze the THz optical response of the asymmetric metasurface. As illustrated by the geometry in Fig. 2(a), this asymmetric metasurface shows no spin-locked optical chirality because the planar metasurface cannot break mirror symmetry due to the limited thickness of the two-dimensional (2D) like metallic layer, so that they cannot achieve far-field optical chirality [20,49]. However, the spin-flipped states exhibit the asymmetric transmission and polarization conversion

effect because this structure breaks the rotational symmetry in the metasurface plane.

We have measured this metasurface with the LP or CP incidence by using the THz-TDPS system, and also simulated this model by using the FDTD method. Figure 3(a) shows the intensity transmission expressed in dB when illuminated by  $x$ -LP and  $y$ -LP light. At the resonant frequency of  $0.6 \text{ THz}$ , the ellipticity for  $x$ -LP illumination can be reached  $34 \text{ dB}$  [orange curves in Fig. 3(c)]. In contrast, the ellipticity under  $y$ -LP illumination is only  $-17 \text{ dB}$  at  $0.68 \text{ THz}$  [blue curves in Fig. 3(c)]. Moreover, the simulated intensity transmission and the ellipticity are shown in Figs. 3(b) and 3(d). Both the experimental and simulated results show that the metasurface can realize the polarization conversion in a certain frequency band. In other words, an incident  $x$ -LP light outputs an RCP light at  $0.6 \text{ THz}$ , and an incident  $y$ -LP light outputs an approximate LCP light at  $0.68 \text{ THz}$ .

Figures 4(a) and 4(b) show the intensity transmission expressed in dB when illuminated by the LCP and RCP light. Both the experimental and simulated results show that the two spin-locked states are almost the same, i.e.,  $T_{RR}^m = T_{LL}^m$ . Thus, the spin-locked CD is nearly 0 in the whole THz frequency band, indicating that the planar metasurface has no optical chirality of the spin-locked state [orange curves in Figs. 4(c) and 4(d)]. In contrast, the intensity transmission of two spin-flipped states is relatively small and not equal to each other, i.e.,  $T_{RL}^m \neq T_{LR}^m$ , due to the polarization conversion of the metasurface. The difference between the two spin-flipped states results in a large spin-flipped CD [blue curves in Figs. 4(c) and 4(d)], which indicates the asymmetric polarization conversion effect. Note that the experimental results are consistent with the simulated results, and the slight difference is mainly due to the error of the fabrication. Therefore, the results of the experiment and simulation confirm the conclusion obtained by geometric symmetry analysis shown in Fig. 2(a), and the

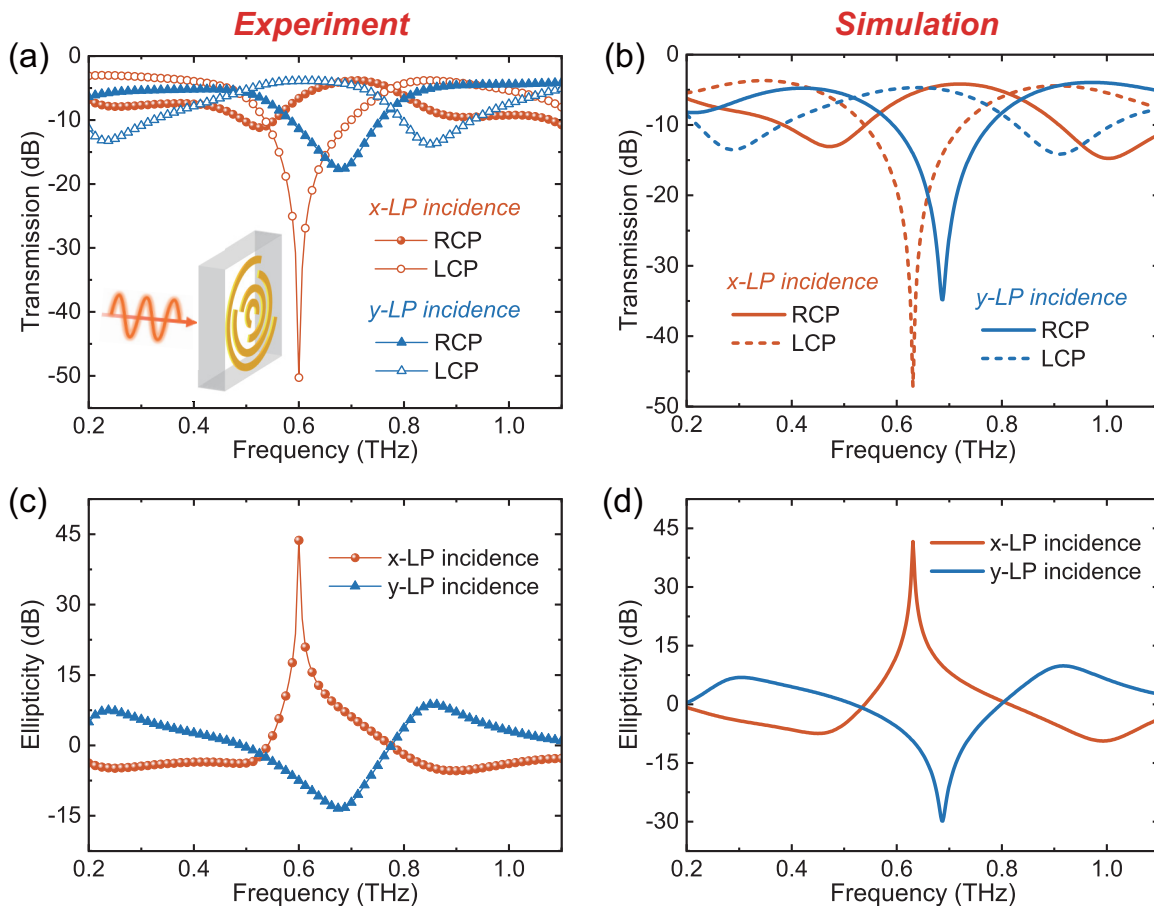


FIG. 3. The experimental RCP and LCP transmission spectra (a) and the ellipticity (c) of the asymmetric metasurface when illuminated by an  $x$ - or  $y$ -LP light. The simulated RCP and LCP transmission spectra (b) and the ellipticity (d) of the asymmetric metasurface when illuminated by an  $x$ - or  $y$ -LP light.

transfer matrix for spin states of this asymmetric metasurface can be modeled as follows:

$$\mathbf{T}^M = \begin{pmatrix} t_{RR}^m & t_{RL}^m \\ t_{LR}^m & t_{LL}^m \end{pmatrix} = \begin{pmatrix} t_{co} & t_{RL}^m \\ t_{LR}^m & t_{co} \end{pmatrix}. \quad (7)$$

### B. Dynamically controlled chirality of LC chiral metasurface

As the LC is a uniaxial birefringent crystal, the refractive index for the extraordinary axis ( $n_e$ ) is different from that of the ordinary axis ( $n_o$ ). The angle between the optical axis of the LC molecule and the  $x$  axis is defined as  $\theta$ . The phase shift  $\delta = 2\pi(n_o - n_e)L/\lambda$ , where  $L = 0.3$  mm is the thickness of the LC layer. Although the LC molecules have some unevenness in this thick LC layer, this unevenness can be ignored compared to a THz wavelength in the submillimeter scale. The LC can still be treated as a homogeneous material for THz waves. Therefore, when the LC molecules are arranged along a certain direction in the  $x$ - $y$  plane, the single LC layer acts as a wave plate or a  $P$ - $B$  phase metasurface with the function of polarization conversion and phase shift [50,51], moreover, the optical axis  $\theta$  of the LC can be actively controlled by the external electric field. In the case of ignoring absorption and

dispersion, the transfer matrix of the LC in the circular vector base can be written as

$$\mathbf{T}^{LC} = \begin{pmatrix} t_{RR}^{LC} & t_{RL}^{LC} \\ t_{LR}^{LC} & t_{LL}^{LC} \end{pmatrix} = \begin{pmatrix} \cos(\frac{\delta}{2}) & ie^{-i2\theta} \sin(\frac{\delta}{2}) \\ ie^{i2\theta} \sin(\frac{\delta}{2}) & \cos(\frac{\delta}{2}) \end{pmatrix}. \quad (8)$$

However, no matter how the optical axis  $\theta$  of the LC rotates in the  $x$ - $y$  plane, there is no optical chirality ( $T_{RR}^{LC} = T_{LL}^{LC}$  and  $T_{LR}^{LC} = T_{RL}^{LC}$ ) since it still has mirror symmetry in the propagation direction. This geometric symmetry is shown in Fig. 2(b). Therefore, there is no optical chirality in either the single asymmetric metasurface or the single anisotropic LC layer.

Next, we discuss the case of introducing the LC layer into the asymmetric metasurface, whose geometric symmetry is illustrated in Fig. 2(c). In this case, the composite structure is no longer regarded as a 2D thin layer geometrically, but a double-layer structure consisting of a rotationally symmetric broken metasurface layer and an LC layer with a geometric  $P$ - $B$  phase. In such a double-layer structure, because the rotational symmetry of one layer is broken and the other layer has uniaxial anisotropy along a certain direction, no matter how this anisotropic axis rotates in the plane, the anisotropic polarization axis of the metasurface layer and the LC layer

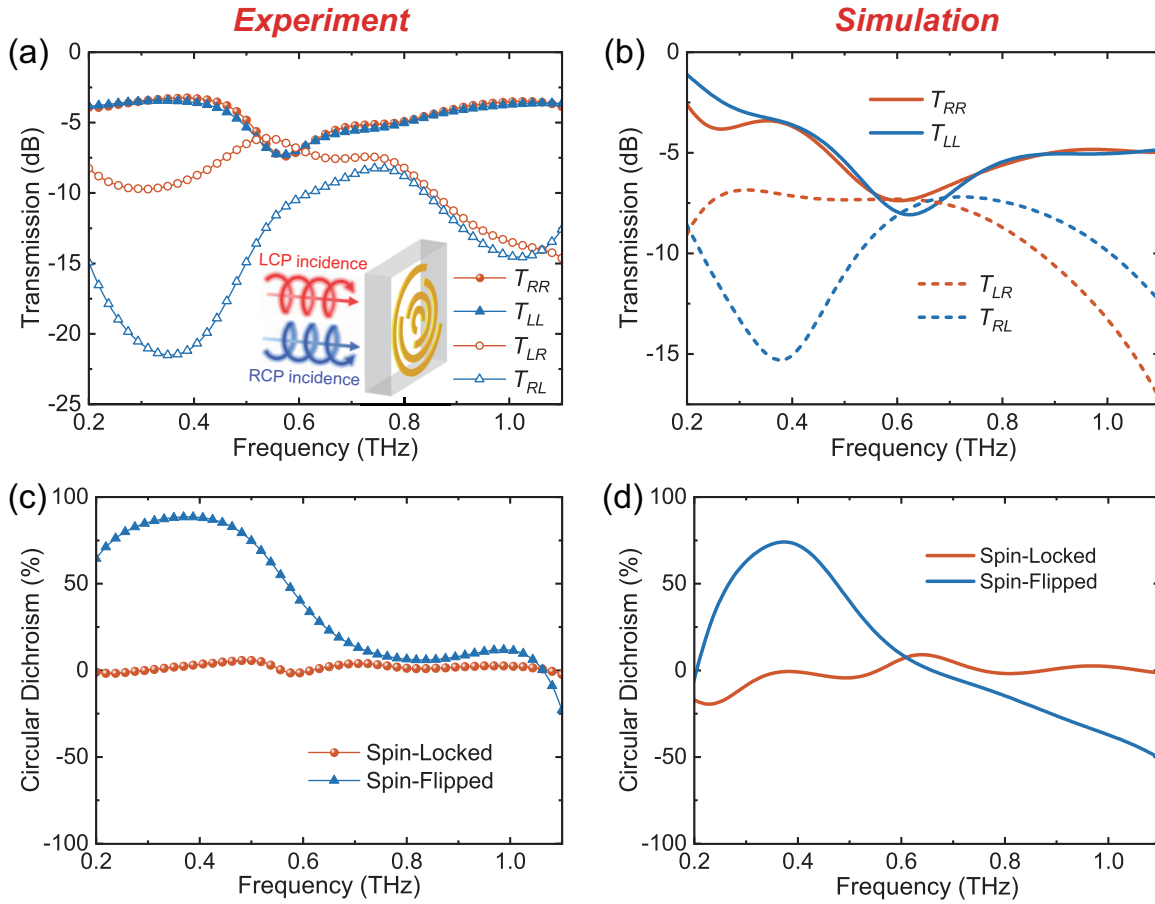


FIG. 4. The experimental transmission spectra (a) and the CD (c) of the spin-locked states and spin-flipped states when illuminated by RCP or LCP light. The simulated transmission spectra (b) and the CD (d) of the spin-locked states and spin-flipped states when illuminated by RCP or LCP light.

always has a certain angle in the THz band, thereby breaking the mirror symmetry along the wave propagation direction [18–21]. Therefore, we can use two achiral structures to form

an active THz chiral meta device. Under the orthogonal CP basis vector, the transfer matrix of the composite LC chiral metasurface is modeled as [52]

$$\begin{aligned} \mathbf{T}^{LCM} &= \mathbf{T}^{LC} \mathbf{T}^M = \begin{pmatrix} \cos(\frac{\delta}{2}) & ie^{-i2\theta} \sin(\frac{\delta}{2}) \\ ie^{i2\theta} \sin(\frac{\delta}{2}) & \cos(\frac{\delta}{2}) \end{pmatrix} \begin{pmatrix} t_{co} & t_{RL}^m \\ t_{LR}^m & t_{co} \end{pmatrix} \\ &= \begin{pmatrix} t_{co} \cos(\frac{\delta}{2}) + it_{LR}^m e^{-i2\theta} \sin(\frac{\delta}{2}) & t_{RL}^m \cos(\frac{\delta}{2}) + it_{co} e^{-i2\theta} \sin(\frac{\delta}{2}) \\ t_{LR}^m \cos(\frac{\delta}{2}) + it_{co} e^{i2\theta} \sin(\frac{\delta}{2}) & t_{co} \cos(\frac{\delta}{2}) + it_{RL}^m e^{i2\theta} \sin(\frac{\delta}{2}) \end{pmatrix}. \end{aligned} \quad (9)$$

It can be seen from Eq. (9) that the phase and amplitude of the transmission coefficients on the two sets of diagonals in the matrix (that is, spin-locked states and spin-flipped states) will change by rotating the optical axis ( $\theta$ ) of the LC layer. Moreover, no matter how the optical axis of the LC molecule rotates, the transmission coefficients of two spin-locked states (or two spin-flipped states) for the composite device do not equal each other (i.e.,  $T_{RR} \neq T_{LL}$ ,  $T_{LR} \neq T_{RL}$ ), which also corresponds to the asymmetric transmission of the spin-locked states (or the spin-flipped states). In this way, the composite device not only exhibits the spin-locked chirality but also the spin-flipped chirality, which is illustrated as Fig. 2(c),

and these chiral effects are actively controlled by electrically rotating the optical axis  $\theta$  of the LC.

Next, we carry out experimental verification. As discussed above in Sec. II B, the polarizer placed in front of the sample rotates to obtain two orthogonal incident waves (that is,  $+45^\circ$ -LP incidence and  $-45^\circ$ -LP incidence). Meanwhile, the polarizer placed behind the sample rotates to obtain two orthogonal LP components of the output THz waves. As a result, the four time-domain signals are obtained, as shown in Fig. 5. When the bias voltage increases from 0 to 300 V, there are obvious changes in the amplitude of the co-LP transmission components [Figs. 5(a) and 5(d)] and the phase of

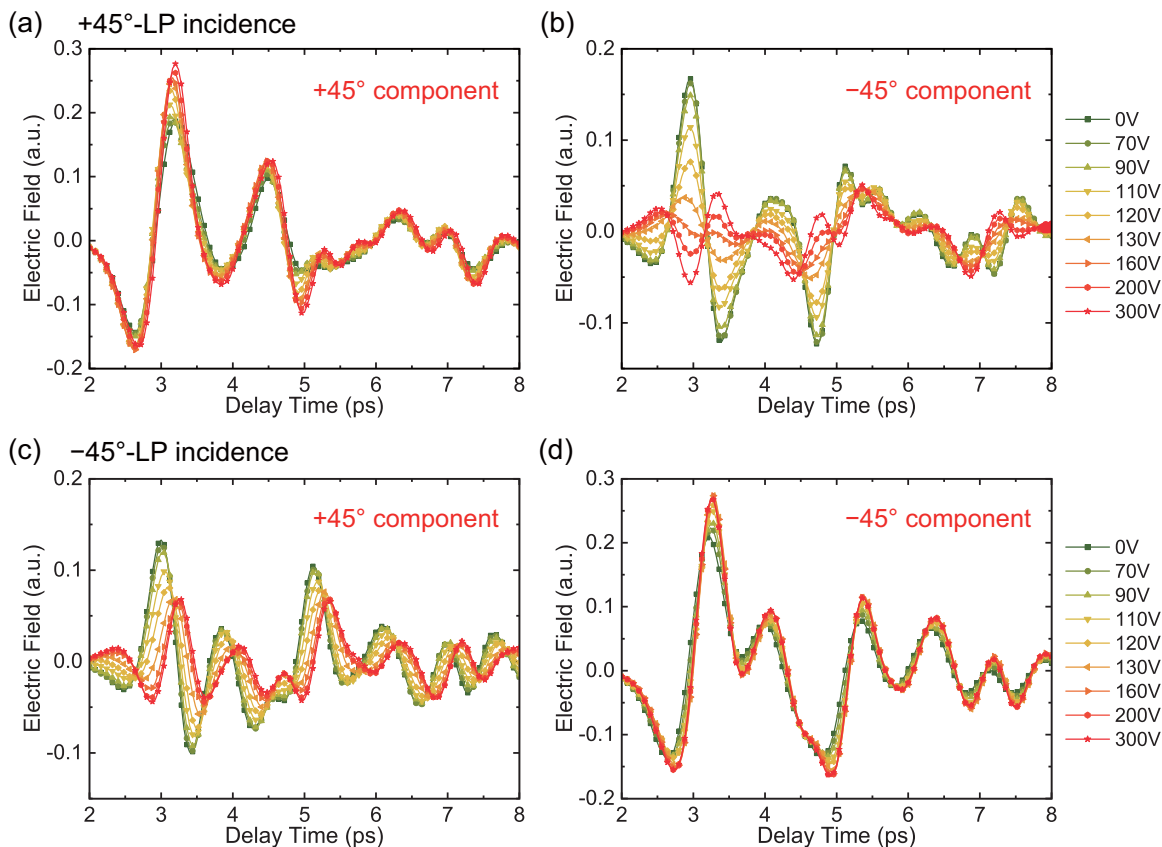


FIG. 5. Experimental THz time-domain signals of the  $+45^\circ$  components (a) and  $-45^\circ$  components (b) with the bias voltage increase from 0 to 300 V when illuminated by a  $+45^\circ$ -LP light. Experimental THz time-domain signals of the  $+45^\circ$  components (c) and  $-45^\circ$  components (d) with the bias voltage increase from 0 to 300 V when illuminated by a  $-45^\circ$ -LP light.

the cross-LP transmission components [Figs. 5(b) and 5(c)]. These changes in the time domain also reflect the dynamically controlling spin state conversion and chirality. After the Fourier transforms, the corresponding amplitude and phase in the frequency domain are obtained, correspondingly. Then, the phase and intensity transmission of the four spin states can be derived by using these data according to Eq. (5), and the intensity transmission spectra are shown in Fig. 6.

As shown in Fig. 6, with the increase of the bias voltage (i.e., the change of the LC optical axis), the transmission spectra of the four spin states are different, and these experimental conclusions are consistent with the above qualitative analysis in the theoretical model described as Eq. (9). Moreover, the obvious differences between the two spin-locked states or the two spin-flipped states give rise to a spin-locked CD (or a spin-flipped CD). The four spin states change continuously with the bias voltage: the resonance frequencies of the  $T_{RR}$  and  $T_{LR}$  are blueshifted as the bias voltage increases from 0 to 300 V when illuminated by RCP light in Figs. 6(a) and 6(b). In Figs. 6(c) and 6(d), the resonance frequencies of the  $T_{LL}$  and  $T_{RL}$  components are redshifted as the bias voltage increases when illuminated by LCP light. The variation of the RCP output ( $T_{RR}$  and  $T_{RL}$ ) was not significant, but the LCP output ( $T_{LL}$  and  $T_{LR}$ ) changed sharply.

Figure 7 shows the simulated intensity transmission when illuminated by RCP or LCP light. As the direction angle of the LCs increases from  $0^\circ$  to  $90^\circ$ , the resonance peak of the

$T_{RR}$  and  $T_{LR}$  components gradually blueshift, and the  $T_{LL}$  and  $T_{RL}$  components gradually redshift. By comparison with the above experimental results in Fig. 6, the simulation results are not perfectly consistent with the experimental results, and the difference between experiment and simulation mainly comes from three points: (i) the absorption and dispersion of the LC are ignored in the simulation; (ii) the rotation angle of the LC optical axis in the simulation cannot perfectly match the actual voltages in the experiment; (iii) the arrangement of LC molecules is not perfect in the experiment. Overall, with the rotation of the optical axis of LC molecules, both the resonance spectral lines and the frequency shifting trend of the four spin states in the simulation shown in Fig. 7 are basically consistent with the experimental results in Fig. 6. Both the experimental and simulated results show that there are obvious differences between the two spin-locked states and also differences between the two spin-flipped states, which give rise to a spin-locked CD (or a spin-flipped CD), indicating that there is a clear optical chirality in the composite structure, which are also consistent with the above qualitative analysis as Fig. 2(c).

To analyze the polarization state of the output light for the CP incidence, we show the ellipticity  $\chi$  for the CP incidence in Fig. 8, which can be obtained by Eq. (3). We note that the resonance in ellipticity is blueshifted from 0.68 to 0.92 THz as the bias voltage increases when illuminated by RCP light [Fig. 8(a)]. Although there is no obvious shift of the resonance

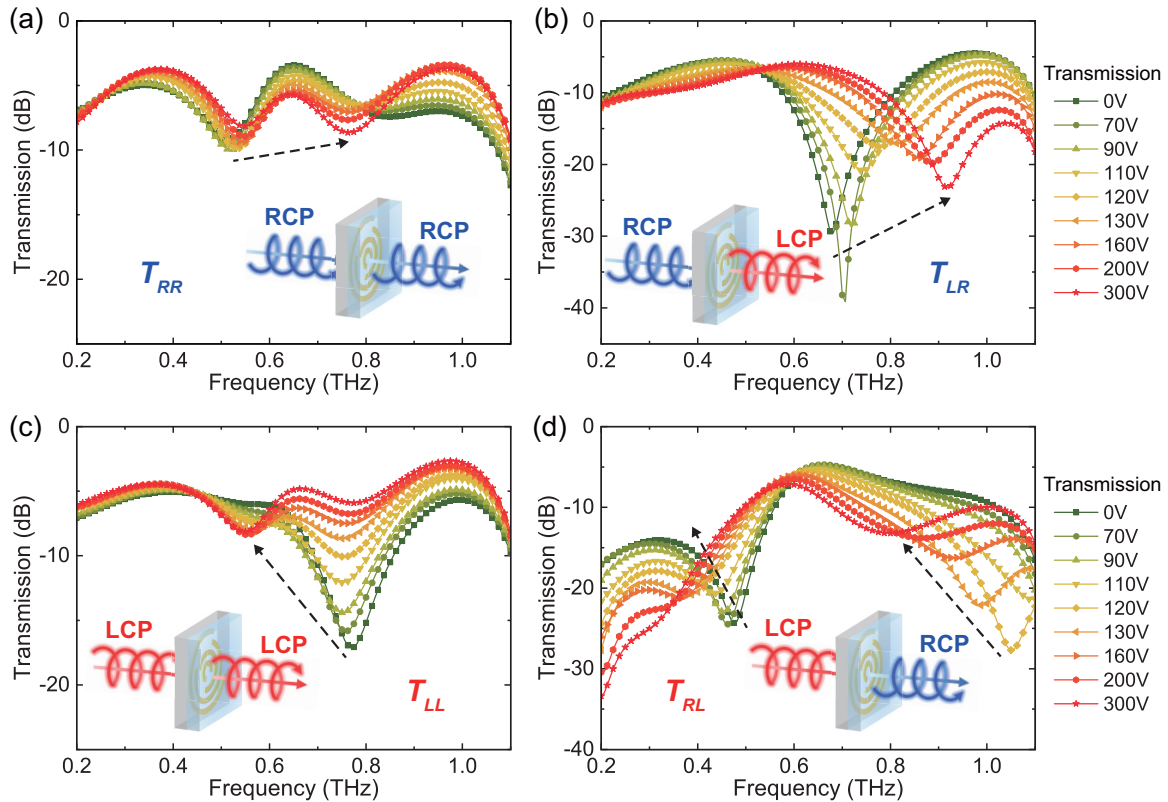


FIG. 6. The experimental transmission spectra  $T_{RR}$  (a),  $T_{LR}$  (b),  $T_{LL}$  (c), and  $T_{RL}$  (d) with the bias voltage increase from 0 to 300 V when illuminated by RCP or LCP light.

peak in ellipticity for LCP illumination, we can still observe the tuning of the ellipticity as the voltage increases [Fig. 8(b)]. According to Eq. (2), we then plot the change process of the output spin state at a certain frequency with the bias voltage increase from 0 to 300 V in Figs. 8(c) and 8(d), and the black dotted line represents the spin state of the incident wave. When illuminated by the RCP state, the output wave gradually changes from an approximate CP light to a perfect LP light with the polarization direction rotated about  $45^\circ$  at 0.71 THz. In contrast, the transition of the output polarization state is relatively small at 1.0 THz, and the polarization angle is also rotated by about  $45^\circ$  [Fig. 8(c)]. As can be seen in Fig. 8(d), the transition of the output polarization state also occurs in the case of LCP illumination. The polarization angle does not rotate at 0.48 THz, whereas the polarization angle rotates about  $80^\circ$  at 1.0 THz. The above results show that this device has a widely tunable polarization conversion function for the different incident polarization states of THz waves by changing the bias voltage continuously. As illustrated in Fig. 1(b), the THz polarization conversion can be controlled between CP to CP (corresponding to the “OFF” state with no applied bias voltage) and CP to LP (corresponding to the “ON” state by applying a bias voltage) when illuminated by a CP light. Essentially, the polarization conversion here originates from the two spin-flipped states in THz spin state conversion (LCP to RCP and RCP to LCP).

Finally, the dynamically controlled THz chirality of the composite LC chiral metasurface can be obtained, as shown in Fig. 9. As previously mentioned, there are not only two spin-locked states but also two spin-flipped states in the trans-

mission signal. More importantly, the different transmission between the two spin-locked states ( $T_{LL}$  and  $T_{RR}$ ) results in a large spin-locked CD, whereas the different transmission between the two spin-flipped states ( $T_{RL}$  and  $T_{LR}$ ) results in a strong spin-flipped CD. The optical chirality of this device leads to different transport properties of four spin states. Take the 0 V and 0.77 THz case as an example; there are two kinds of asymmetric transmission for the spin states: on the one hand, the incidence of the RCP state can output the RCP state, but the LCP cannot output the LCP; on the other hand, the incident RCP state cannot be converted into LCP output, but LCP incidence can be converted to RCP output. At 200 V, the optical chirality almost disappeared, so both RCP and LCP can be directly output, but both cannot be converted to the opposite chiral state output.

From Fig. 9(a), there are two distinct resonances in the CD spectrum for the spin-locked state at around 0.5 and 0.77 THz. As the bias voltage increases from 0 to 300 V, the resonance intensity in the CD spectrum for the spin-locked state gradually decreases and then flips slightly with a large controllable range of 83.8% to  $-30.7\%$  of the spin-locked CD at 0.76 THz. A similar trend is found in the OA spectrum, where the two distinct resonances are around 0.6 and 0.83 THz [Fig. 9(c)]. For the spin-flipped state, both the CD and OA are attributed to the asymmetric transmission behavior of the converted components for the spin states of opposite handedness, and the large controllable range of spin-flipped CD at 0.73 THz is from  $-98.2\%$  to  $44.7\%$  as the bias voltage increases [Fig. 9(b)]. The spin-flipped OA also has electrically controllable tunability, as shown in Fig. 9(d). These



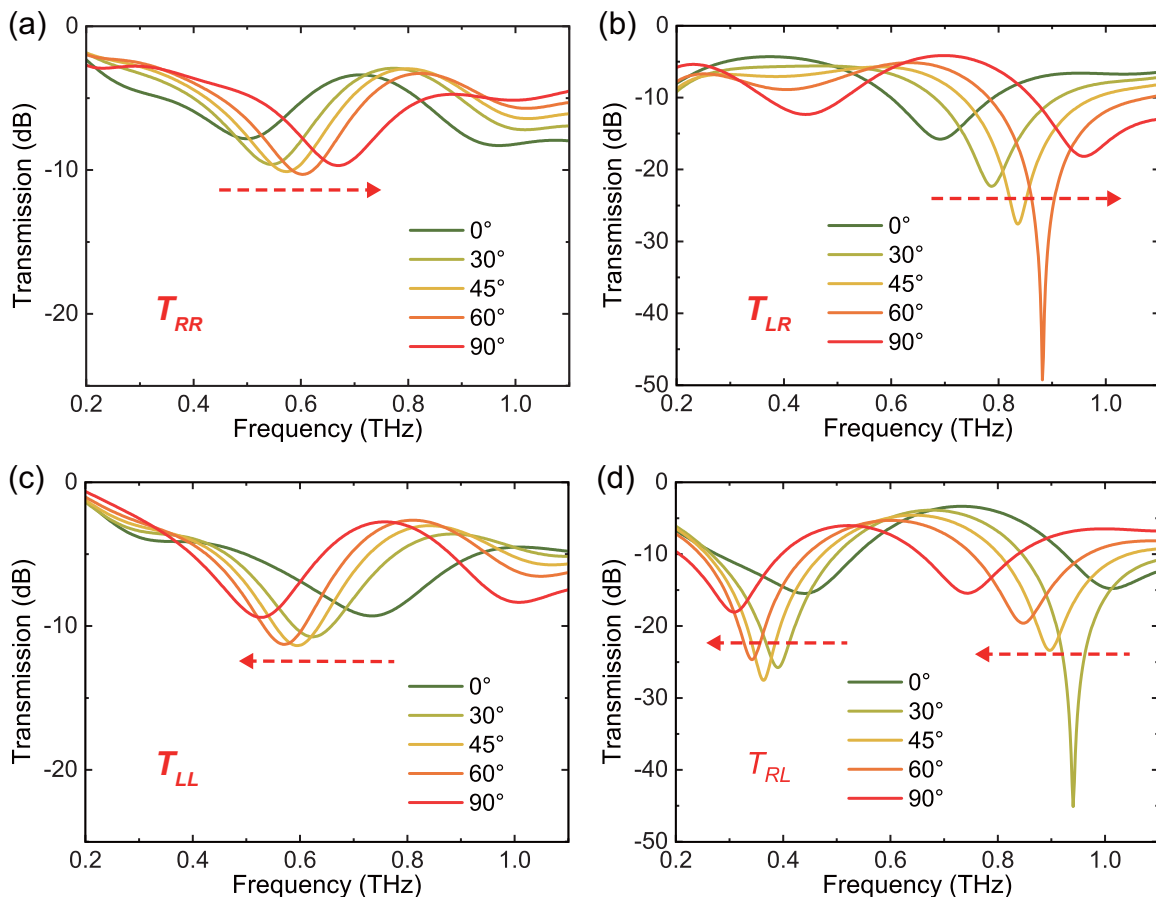


FIG. 7. The simulated transmission spectra  $T_{RR}$  (a),  $T_{LR}$  (b),  $T_{LL}$  (c), and  $T_{RL}$  (d) with the angle increase from  $0^\circ$  to  $90^\circ$  when illuminated by RCP or LCP light.

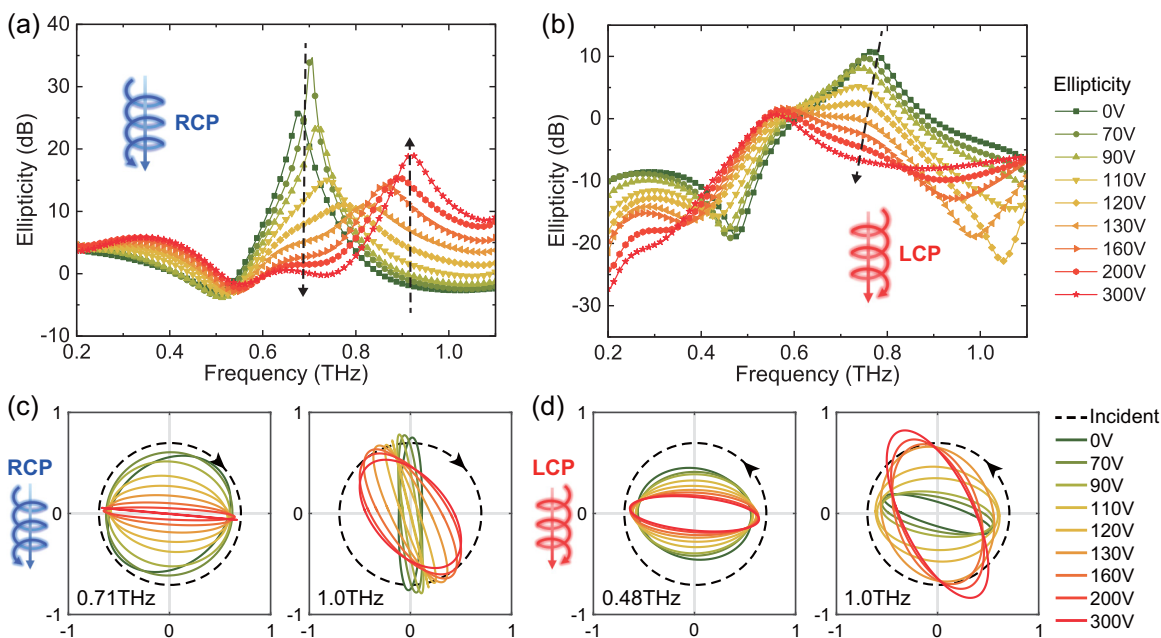


FIG. 8. The ellipticity of the composite LC chiral metasurface with the bias voltage increase from 0 to 300 V when illuminated by RCP light (a) or LCP light (b). (c) Output polarization states at 0.71 and 1.0 THz with the bias voltage increase from 0 to 300 V when illuminated by RCP light. (d) Output polarization states at 0.48 and 1.0 THz with the bias voltage increase from 0 to 300 V when illuminated by LCP light.

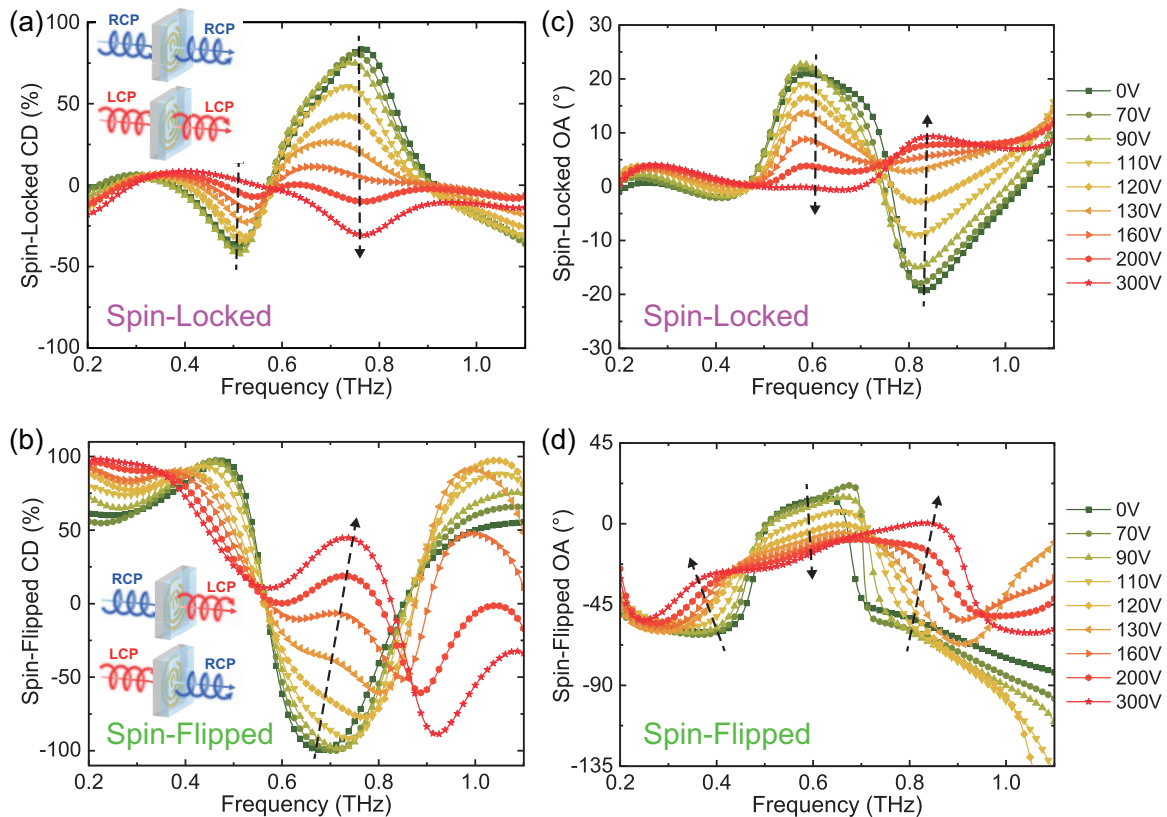


FIG. 9. The spin-locked CD (a) and spin-locked OA (c) with the bias voltage increase from 0 to 300 V when illuminated by RCP or LCP light. The spin-flipped CD (b) and spin-flipped OA (d) with the bias voltage increase from 0 to 300 V when illuminated by RCP or LCP light.

dynamically controlled chiral effects are also consistent with the above qualitative theoretical analysis described as Eq. (9). Moreover, in the Supplemental Material [53], we show that the experimental results meet both the Lorentz reciprocity of this device and the Kramers-Kronig relation between the CD and OA, which proves the reliability of the experimental measurement method.

Finally, compared to the previous reports on active THz chiral devices discussed in Sec. I [31–37], the working mechanism in most of these devices is as follows: the THz chirality is totally generated by the artificial microstructure, and the active control is realized by the free carrier excitation in the additional materials, such as graphene or  $\text{VO}_2$ , so that the intensity modulating or switching CD value can be realized. In contrast, the THz chirality of our device is excited by the combination of both the metasurface and LC anisotropies, and the optical axis rotation of the LC also provides an active tuning mechanism. Therefore, both the generation and tuning mechanisms of THz chirality in this device are quite different from those of the previous reports. This device brings multi-functional manipulations of THz polarization and chirality.

#### IV. CONCLUSION

In summary, we have demonstrated an active THz chiral device based on the combination of the asymmetric metasurface and the LC, of which the spin state conversion and

optical chirality can be flexibly manipulated by electrically controlling the optical axis of the anisotropic LC layer. This composite structure not only exhibits spin state conversion, but also generates spin-locked chirality and spin-flipped chirality by breaking the mirror symmetry. The results show that this device has a widely tunable polarization conversion (e.g., switching between CP to CP and CP to LP for CP illumination) and a dynamically controlled chiral asymmetric transmission for the THz waves, of which a large controllable range of 83.8% to  $-30.7\%$  for the spin-locked CD at 0.76 THz and a broad range of  $-98.2\%$  to 44.7% for the spin-flipped CD at 0.73 THz are achieved. Our approach of using asymmetric metasurface integrated with LCs provides a simple and flexible method in the dynamic manipulation of THz spin state and chirality, which may lead to various applications in THz technologies, such as active polarization modulation of THz waves and polarization-sensitive or chiral-sensitive THz detection.

#### ACKNOWLEDGMENTS

This work was supported by the National Natural Science Foundation of China (Grants No. 61971242 and No. 61831012), the National Key Research and Development Program of China (Grant No. 2017YFA0701000), and the Natural Science Foundation of Tianjin City (Grant No. 19JCY-BJC16600).

- [1] M. Hentschel, M. Schäferling, T. Weiss, N. Liu, and H. Giessen, Three-dimensional chiral plasmonic oligomers, *Nano Lett.* **12**, 2542 (2012).
- [2] Y. Luo, C. Chi, M. Jiang, R. Li, S. Zu, Y. Li, and Z. Fang, Plasmonic chiral nanostructures: Chiroptical effects and applications, *Adv. Opt. Mater.* **5**, 1700040 (2017).
- [3] M. A. Cole, W.-c. Chen, M. Liu, S. S. Kruk, W. J. Padilla, I. V. Shadrivov, and D. A. Powell, Strong Broadband Terahertz Optical Activity Through Control of the Blaschke Phase With Chiral Metasurfaces, *Phys. Rev. Appl.* **8**, 014019 (2017).
- [4] M. Hentschel, M. Schäferling, X. Duan, H. Giessen, and N. Liu, Chiral plasmonics, *Sci. Adv.* **3**, e1602735 (2017).
- [5] V. S. Asadchy, C. Guo, I. A. Faniayeu, and S. Fan, Three-dimensional random dielectric colloid metamaterial with giant isotropic optical activity, *Laser Photon. Rev.* **14**, 2000151 (2020).
- [6] G. D. Fasman, *Circular Dichroism and the Conformational Analysis of Biomolecules* (Springer, Boston, 1996).
- [7] L. D. Barron, *Molecular Light Scattering and Optical Activity*, 2nd ed. (Cambridge University Press, Cambridge, UK, 2004).
- [8] M. Schäferling, *Chiral Nanophotonics* (Springer, Switzerland, 2017).
- [9] Y. Tang and A. E. Cohen, Optical Chirality and its Interaction with Matter, *Phys. Rev. Lett.* **104**, 163901 (2010).
- [10] E. Plum, V. A. Fedotov, A. S. Schwanecke, N. I. Zheludev, and Y. Chen, Giant optical gyrotropy due to electromagnetic coupling, *Appl. Phys. Lett.* **90**, 223113 (2007).
- [11] A. Kuzyk, R. Schreiber, Z. Fan, G. Pardatscher, E.-M. Roller, A. Högele, F. C. Simmel, A. O. Govorov, and T. Liedl, DNA-based self-assembly of chiral plasmonic nanostructures with tailored optical response, *Nature (London)* **483**, 311 (2012).
- [12] B. Frank, X. Yin, M. Schäferling, J. Zhao, S. M. Hein, P. V. Braun, and H. Giessen, Large-area 3D chiral plasmonic structures, *ACS Nano* **7**, 6321 (2013).
- [13] C. He, T. Sun, J. Guo, M. Cao, J. Xia, J. Hu, Y. Yan, and C. Wang, Chiral metalens of circular polarization dichroism with helical surface arrays in mid-infrared region, *Adv. Opt. Mater.* **7**, 1901129 (2019).
- [14] R. Singh, E. Plum, C. Menzel, C. Rockstuhl, A. K. Azad, R. A. Cheville, F. Lederer, W. Zhang, and N. I. Zheludev, Terahertz metamaterial with asymmetric transmission, *Phys. Rev. B* **80**, 153104 (2009).
- [15] L. Cong, P. Pitchappa, N. Wang, and R. Singh, Electrically programmable terahertz diatomic metamolecules for chiral optical control, *Research* **2019**, 7084251 (2019).
- [16] A. V. Rogacheva, V. A. Fedotov, A. S. Schwanecke, and N. I. Zheludev, Giant Gyrotropy Due to Electromagnetic-Field Coupling in a Bilayered Chiral Structure, *Phys. Rev. Lett.* **97**, 177401 (2006).
- [17] T. Q. Li, H. Liu, T. Li, S. M. Wang, F. M. Wang, R. X. Wu, P. Chen, S. N. Zhu, and X. Zhang, Magnetic resonance hybridization and optical activity of microwaves in a chiral metamaterial, *Appl. Phys. Lett.* **92**, 131111 (2008).
- [18] C. Helgert, E. Pshenay-Severin, M. Falkner, C. Menzel, C. Rockstuhl, E.-B. Kley, A. Tünnermann, F. Lederer, and T. Pertsch, Chiral metamaterial composed of three-dimensional plasmonic nanostructures, *Nano Lett.* **11**, 4400 (2011).
- [19] S. Zu, Y. Bao, and Z. Fang, Planar plasmonic chiral nanostructures, *Nanoscale* **8**, 3900 (2016).
- [20] A. Y. Zhu, W. T. Chen, A. Zaidi, Y.-W. Huang, M. Khorasaninejad, V. Sanjeev, C.-W. Qiu, and F. Capasso, Giant intrinsic chiro-optical activity in planar dielectric nanostructures, *Light: Sci. Appl.* **7**, 17158 (2018).
- [21] S. Nechayev, R. Barczyk, U. Mick, and P. Banzer, Substrate-induced chirality in an individual nanostructure, *ACS Photonics* **6**, 1876 (2019).
- [22] M. Liu, E. Plum, H. Li, S. Duan, S. Li, Q. Xu, X. Zhang, C. Zhang, C. Zou, B. Jin *et al.*, Switchable Chiral Mirrors, *Adv. Opt. Mater.* **8**, 2000247 (2020).
- [23] T. Cao, Y. Li, X. Zhang, and Y. Zou, Theoretical study of tunable chirality from graphene integrated achiral metasurfaces, *Photon. Res.* **5**, 441 (2017).
- [24] D. Xiao, Y. J. Liu, S. Yin, J. Liu, W. Ji, B. Wang, D. Luo, G. Li, and X. W. Sun, Liquid-crystal-loaded chiral metasurfaces for reconfigurable multiband spin-selective light absorption, *Opt. Express* **26**, 25305 (2018).
- [25] R. Damari, O. Weinberg, D. Krotkov, N. Demina, K. Akulov, A. Golombek, T. Schwartz, and S. Fleischer, Strong coupling of collective intermolecular vibrations in organic materials at terahertz frequencies, *Nat. Commun.* **10**, 3248 (2019).
- [26] M. R. Ryder, B. Van de Voorde, B. Civalieri, T. D. Bennett, S. Mukhopadhyay, G. Cinque, F. Fernandez-Alonso, D. De Vos, S. Rudić, and J.-C. Tan, Detecting Molecular Rotational Dynamics Complementing the Low-Frequency Terahertz Vibrations in a Zirconium-Based Metal-Organic Framework, *Phys. Rev. Lett.* **118**, 255502 (2017).
- [27] D. Hou, X. Li, J. Cai, Y. Ma, X. Kang, P. Huang, and G. Zhang, Terahertz spectroscopic investigation of human gastric normal and tumor tissues, *Phys. Med. Biol.* **59**, 5423 (2014).
- [28] L. Yu, L. Hao, T. Meiqiong, H. Jiaoqi, L. Wei, D. Jinying, C. Xueping, F. Weiling, and Z. Yang, The medical application of terahertz technology in non-invasive detection of cells and tissues: Opportunities and challenges, *RSC Adv.* **9**, 9354 (2019).
- [29] W. J. Choi, G. Cheng, Z. Huang, S. Zhang, T. B. Norris, and N. A. Kotov, Terahertz circular dichroism spectroscopy of biomaterials enabled by kirigami polarization modulators, *Nat. Mater.* **18**, 820 (2019).
- [30] J. Cheng, R. C. Jones, O. Sushko, Y. Tashiro, and R. Donnan, Quasi-optical sub-THz circular dichroism spectroscopy of solvated myoglobin, *IEEE Trans. Terah. Sci. Technol.* **10**, 348 (2020).
- [31] S. Zhang, J. Zhou, Y.-S. Park, J. Rho, R. Singh, S. Nam, A. K. Azad, H.-T. Chen, X. Yin, A. J. Taylor *et al.*, Photoinduced handedness switching in terahertz chiral metamolecules, *Nat. Commun.* **3**, 942 (2012).
- [32] J. Zhou, D. R. Chowdhury, R. Zhao, A. K. Azad, H.-T. Chen, C. M. Soukoulis, A. J. Taylor, and J. F. O'Hara, Terahertz chiral metamaterials with giant and dynamically tunable optical activity, *Phys. Rev. B* **86**, 035448 (2012).
- [33] N. Kanda, K. Konishi, and M. Kuwata-Gonokami, All-photoinduced terahertz optical activity, *Opt. Lett.* **39**, 3274 (2014).
- [34] T. T. Lv, Y. X. Li, H. F. Ma, Z. Zhu, Z. P. Li, C. Y. Guan, J. H. Shi, H. Zhang, and T. J. Cui, Hybrid metamaterial switching for manipulating chirality based on VO<sub>2</sub> phase transition, *Sci. Rep.* **6**, 23186 (2016).
- [35] S. Wang, L. Kang, and D. H. Werner, Active terahertz chiral metamaterials based on phase transition of vanadium dioxide (VO<sub>2</sub>), *Sci. Rep.* **8**, 189 (2018).

- [36] T.-T. Kim, S. S. Oh, H.-D. Kim, H. S. Park, O. Hess, B. Min, and S. Zhang, Electrical access to critical coupling of circularly polarized waves in graphene chiral metamaterials, *Sci. Adv.* **3**, e1701377 (2017).
- [37] S. J. Kindness, N. W. Almond, W. Michailow, B. Wei, K. Delfanazari, P. Braeuninger-Weimer, S. Hofmann, H. E. Beere, D. A. Ritchie, and R. Degl'Innocenti, A terahertz chiral metamaterial modulator, *Adv. Opt. Mater.* **8**, 2000581 (2020).
- [38] G. Isic, B. Vasic, D. C. Zografopoulos, R. Beccherelli, and R. Gajic, Electrically Tunable Critically Coupled Terahertz Metamaterial Absorber Based On Nematic Liquid Crystals, *Phys. Rev. Appl.* **3**, 064007 (2015).
- [39] Z.-X. Shen, S.-H. Zhou, S.-J. Ge, W. Hu, and Y.-Q. Lu, Liquid crystal enabled dynamic cloaking of terahertz Fano resonators, *Appl. Phys. Lett.* **114**, 041106 (2019).
- [40] B. Vasić, G. Isić, R. Beccherelli, and D. C. Zografopoulos, Tunable beam steering at terahertz frequencies using reconfigurable metasurfaces coupled with liquid crystals, *IEEE J. Sel. Top. Quantum Electron.* **26**, 7701609 (2020).
- [41] J. Wu, Z. Shen, S. Ge, B. Chen, Z. Shen, T. Wang, C. Zhang, W. Hu, K. Fan, W. Padilla *et al.*, Liquid crystal programmable metasurface for terahertz beam steering, *Appl. Phys. Lett.* **116**, 131104 (2020).
- [42] O. Buchnev, N. Podoliak, K. Kaltenecker, M. Walther, and V. A. Fedotov, Metasurface-based optical liquid crystal cell as an ultrathin spatial phase modulator for THz applications, *ACS Photonics* **7**, 3199 (2020).
- [43] G. Isić, D. C. Zografopoulos, D. B. Stojanović, B. Vasić, and M. R. Belić, Beam steering efficiency in resonant reflective metasurfaces, *IEEE J. Sel. Top. Quantum Electron.* **27**, 4700208 (2021).
- [44] X. Zhang, F. Fan, Y.-Y. Ji, and S.-J. Chang, Temperature-dependent chirality of cholesteric liquid crystal for terahertz waves, *Opt. Lett.* **45**, 4988 (2020).
- [45] H. G. Berry, G. Gabrielse, and A. E. Livingston, Measurement of the Stokes parameters of light, *Appl. Opt.* **16**, 3200 (1977).
- [46] C. Menzel, C. Rockstuhl, and F. Lederer, Advanced Jones calculus for the classification of periodic metamaterials, *Phys. Rev. A* **82**, 053811 (2010).
- [47] Z. Wang, F. Cheng, T. Winsor, and Y. Liu, Optical chiral metamaterials: A review of the fundamentals, fabrication methods and applications, *Nanotechnology* **27**, 412001 (2016).
- [48] S. Liu, L. Zhang, Q. L. Yang, Q. Xu, Y. Yang, A. Noor, Q. Zhang, S. Iqbal, X. Wan, Z. Tian *et al.*, Frequency-Dependent Dual-Functional Coding Metasurfaces at Terahertz Frequencies, *Adv. Opt. Mater.* **4**, 1965 (2016).
- [49] E. Plum, X.-X. Liu, V. A. Fedotov, Y. Chen, D. P. Tsai, and N. I. Zheludev, Metamaterials: Optical Activity Without Chirality, *Phys. Rev. Lett.* **102**, 113902 (2009).
- [50] X. Zhang, S. Yang, W. Yue, Q. Xu, C. Tian, X. Zhang, E. Plum, S. Zhang, J. Han, and W. Zhang, Direct polarization measurement using a multiplexed Pancharatnam-Berry metahologram, *Optica* **6**, 1190 (2019).
- [51] X. Yin, Z. Ye, J. Rho, Y. Wang, and X. Zhang, Photonic spin hall effect at metasurfaces, *Science* **339**, 1405 (2013).
- [52] R. Zhang, Q. Zhao, X. Wang, J. Li, and W. Y. Tam, Circular phase-dichroism of chiral metasurface using birefringent interference, *Nano Lett.* **20**, 2681 (2020).
- [53] See Supplemental Material at <http://link.aps.org/supplemental/10.1103/PhysRevMaterials.5.085201> for additional details regarding Lorentz reciprocity characteristic and Kramers-Kronig relation of the composite liquid crystal chiral metasurface (Figs. S1 and S2). S1: Lorentz reciprocity characteristic. S2: Kramers-Kronig relation. Supplemental Material includes additional Ref. [54].
- [54] M. V. Gorkunov, V. E. Dmitrienko, A. A. Ezhov, V. V. Artemov, and O. Y. Rogov, Implications of the causality principle for ultra chiral metamaterials, *Sci. Rep.* **5**, 9273 (2015).